The Astrophysical Journal, 959:129 (12pp), 2023 December 20 https://doi.org/10.3847/1538-4357/ad0be1

The Effect of Angular Scattering Imposed by Charge Exchange and Elastic Collisions on Interstellar Neutral Hydrogen Atoms

F. Rahmanifard[1], P. Swaczyna[2,3], E. J. Zirnstein[2], J. Heerikhuisen[4], A. Galli[5], J. M. Sokół[6], N. A. Schwadron[1], E. Möbius[1], D. J. McComas[2], and S. A. Fuselier[6,7]
[1] Physics Department, Space Science Center, University of New Hampshire, Durham, NH 03824, USA
[2] Department of Astrophysical Sciences, Princeton University, Princeton, NJ 08544, USA
[3] Space Research Centre PAS (CBK PAN), 00-716 Warsaw, Poland
[4] Department of Mathematics and Statistics, University of Waikato, Hamilton, New Zealand
[5] Physics Institute, University of Bern, Bern, 3012, Switzerland
[6] Southwest Research Institute, San Antonio, TX 78228, USA
[7] University of Texas at San Antonio, San Antonio, TX 78228, USA
Received 2023 June 5; revised 2023 November 6; accepted 2023 November 11; published 2023 December 14

Abstract

Angular scattering (AS) in charge exchange and elastic collisions between interstellar ions and neutral (ISN) atoms has been assumed to be negligible in previous studies. Here, we investigate the momentum transfer associated with the AS of H atoms using Monte Carlo calculations to simulate their transport through the outer heliosheath. We consider two cases where charge exchange and elastic collisions between ISN H atoms and protons occur with and without AS in the outer heliosheath. We show that considering AS decelerates and heats primary ISN H, reducing the effect of selective charge exchange in the outer heliosheath. Secondary ISN H atoms, on the other hand, are not significantly affected by AS. We then simulate the transport of ISN H atoms inside the heliosphere to simulate count rates observed in the lowest energy bin of IBEX-Lo. We study the effect of radiation pressure on the ISN H measurements for the cases with and without AS and compare them with our previous findings. We find an effective radiation parameter ($\mu_{\rm eff}$, which represents force associated with radiation pressure relative to gravity) for the years 2009–2018 based on the longitudinal shift of the ISN H signal. The two cases with and without AS reproduce the longitudinal shift in accordance with variations in solar activity, in agreement with our previous results, and they result in similar values for the $\mu_{\rm eff}$, which is ∼22%–23% larger than the value found based on solar Lyα profile observations.

Unified Astronomy Thesaurus concepts: Heliosphere (711); Heliosheath (710); Solar activity (1475); Interstellar medium (847); Interstellar medium wind (848); Solar wind (1534); Interstellar atomic gas (833); Space plasmas (1544); Collision physics (2065)

1. Introduction

IBEX-Lo is designed to detect interstellar neutral (ISN) atoms from the vantage point of elliptical orbits around Earth, i.e., at 1 au (Fuselier et al. 2009; McComas et al. 2009). The ISN observation season occurs each year from December through April when the Earth and IBEX move into the approaching ISN flow, increasing the incident atoms relative velocity, and thus energy in the spacecraft reference frame. This mission is designed so that the instrument's field of view remains perpendicular to near Sun-pointing (with maximum ∼4°–7° off for each orbit) spin axis. As a consequence, ISN atoms are expected to be detected close to their trajectory perihelion so that their radial velocity is close to zero as they enter the instrument's narrow field of view. The angular distribution of observed ISN fluxes is essential for analyzing ISN flow parameters.

Our very local interstellar medium (VLISM) is believed to be an interaction region between the local interstellar cloud (LIC) and galactic (G) cloud (Swaczyna et al. 2022b). Therefore, it is important to investigate the VLISM through its messengers (the ISN atoms and energetic neutral atoms (ENAs)). Investigating parameters associated with the ISN flow has been important for understanding the VLISM (Möbius et al. 2004). A Maxwellian may adequately describe the ISN distribution in the VLISM far away from the Sun, where its ionized and neutral parts are coupled through charge exchange and elastic collisions. However, encountering the heliosphere heats, decelerates, and diverts the plasma part, forming a bow shock (or bow wave, see McComas et al. 2012; Zank et al. 2013; Fraternale et al. 2023). The neutral part, on the other hand, enters the outer heliosheath partially decoupled from the plasma part and with less significant changes.

Collisions between ions and neutral atoms in the outer heliosheath are not sufficient to maintain thermalization, leading to the decoupling of the plasma and neutral part (Baranov & Malama 1993; Pogorelov et al. 2009). The charge exchange collisions lead to the depletion of the pristine (primary) population and the creation of a secondary population with different thermodynamic properties. Previous models did not include the effect of angular scattering (AS) and the resulting momentum transfer between ions and neutral atoms, assuming it to be negligible. However, for ISN He, this AS significantly alters the distribution function of both primary and secondary populations, particularly leading to a noticeable deviation from the pristine Maxwellian distribution for the primary ISN He (Swaczyna et al. 2023a).

Inside the heliosphere, modification of the ISN atoms' distribution function by the gravitational force from the Sun and ionization processes continues and increases closer to the Sun. Radiation pressure exerted on the ISN H atoms due to resonant absorption and reemission of Lyα further decelerates them. Therefore, while the primary ISN He and O atoms, as well as ISN Ne atoms, have similar bulk speeds and their mean energies at 1 au scale with their mass, the only exception is ISN H. Various He observations obtained the ISN inflow speed $\sim$25–27 km s^{-1} at the edge of the heliosphere (Vallerga et al. 2004; Witte 2004; Bzowski et al. 2014, 2015; McComas et al. 2015; Schwadron et al. 2015; Wood et al. 2015). The other parameters that describe the ISN flow distribution function at the edge of the heliosphere include the temperature, density, and direction (Lallement & Bertin 1992; Linsky et al. 1993; Gloeckler et al. 2004; Möbius et al. 2004). The interstellar magnetic field further provides invaluable information about the interaction of our heliosphere with the surrounding interstellar medium (Izmodenov & Alexashov 2015; Zirnstein et al. 2016; Izmodenov & Alexashov 2020).

IBEX provided the first direct measurements of ISN H (Möbius et al. 2009) and the first measurements of ISN H and He throughout a full solar cycle (Galli et al. 2019; Swaczyna et al. 2022a; Schwadron et al. 2022). The analysis of ISN He observations from IBEX has provided the latest estimates for the unperturbed ISN parameters as reported by Swaczyna et al. (2022a) and Schwadron et al. (2022). The analysis of ISN H data over several years (Saul et al. 2012, 2013) and a full solar cycle (Galli et al. 2019; Rahmanifard et al. 2019) showed their variations with solar activity. Furthermore, investigating the ISN signal over different phases of solar activity demonstrated the effect of radiation pressure on the ISN H signal (Schwadron et al. 2013; Katushkina et al. 2015; Kowalska-Leszczynska et al. 2018a), namely a longitudinal shift of the ISN H signal with increasing solar activity (Zirnstein et al. 2013; Rahmanifard et al. 2019; Katushkina et al. 2021).

ISN H and He are both detected by IBEX-Lo through registering H^- ions either converted from incoming ISN H atoms or sputtered from the conversion surface (Wurz et al. 1997, 2008; Fuselier et al. 2009; Swaczyna et al. 2023b). Therefore, retrieving ISN H count rates from H^- ions presents a challenge and requires further data analysis. This analysis is mostly focused on the effect of radiation pressure, which shifts the ISN H signal in longitude and separates the two signal peaks (Schwadron et al. 2013). While this separation is present throughout different phases of a solar cycle, it increases with solar activity. Galli et al. (2019) explored several retrieval methods by analyzing H^- and O^- count rates during different phases of the observation season when we expect to observe secondary He, primary He, and H signals. They confirmed the basic finding of Saul et al. (2012, 2013) and Schwadron et al. (2013), i.e., that the observation of higher ISN H count rates in energy step (E-Step) 1 (centered at 15 eV) than in E-Step 2 (29 eV) does not depend on the retrieval method.

The larger-than-unity ratio between E-Steps 1 and 2 has led to a discrepancy between IBEX data and existing models. This discrepancy was first reported by Katushkina et al. (2015), where they showed that, contrary to IBEX data, their model obtains higher count rates for ISN H in E-Step 2 than E-Step 1, in the expected radiation pressure and ionization rate range. The same discrepancy has been reported in comparison with other models, including the analytical full integration model (aFINM; Rahmanifard et al. 2019) and the Warsaw Test Particle Model (Galli et al. 2019). To sidestep the discrepancy, Rahmanifard et al. (2019) developed a methodology to use the longitudinal shift in the ISN H signal peak and its variation with solar activity. While increasing the radiation parameter (Kowalska-Leszczynska et al. 2018a; Kowalska-Leszczynska et al. 2018b; Kowalska-Leszczynska et al. 2022) compared to solar Lyα observations (possibly associated with an absolute calibration issue with solar Lyα irradiance observations) may partially address this discrepancy, it is still unresolved.

In this study, we use the same methodology as in Rahmanifard et al. (2019), to investigate the longitudinal shift of the ISN H signal throughout the years 2009–2018. However, we use a modified version of aFINM which is paired with a global heliospheric model to get a more accurate distribution function at the heliospheric boundary. This global model is described in Section 2, where we investigate collisions of ISN H atoms in the outer heliosheath and how they alter the distribution of H atoms at a fiducial boundary of 100 au from the Sun (i.e., near the solar wind termination shock). In Section 2.1 we provide a detailed description of our numerical method. We further compare the two cases with and without considering AS in Section 2.2. In Section 3, we introduce our simulation tool inside 100 au (aFINM), briefly describing how it has been modified and paired with the global model for this study. We further discuss our methodology to find an effective μ parameter for each year based on an agreement with the longitudinal shift of the ISN H signal (Section 3.1). In Section 3.2, we present the results of our ISN H analysis through the years 2009–2018 and compare our results for three cases where we used the 2019 version of the aFINM (hereafter aFINM2019), and the modified version with and without AS. We provide a brief discussion and concluding remarks in Section 4. Furthermore, we list the boundary conditions of the global model in Appendix A and derive analytic distributions for the obtained distribution function at 100 au in Appendix B.

2. Collisions of ISN Hydrogen Atoms in the Outer Heliosheath

This section presents how we calculate the change of the ISN hydrogen distribution function in the outer heliosheath. We use a Monte Carlo approach, for which numbers of the test atom trajectories in analyzed volumes need to be sufficient in order to obtain statistics needed to characterize the distribution functions used later as an input for the second stage calculations (Section 3). Therefore, the boundary of these calculations should be within the heliosphere to account for all outer heliosheath collisions but as large as possible to improve the statistics. We select a sphere at 100 au from the Sun in order to make future comparisons convenient. While a slightly larger sphere would fit the implemented model, the 100 au sphere should be within the heliosphere even under other boundary conditions. While some collisions may still occur in the inner heliosheath, they are less frequent due to lower plasma density. Closer to the Sun, the density increases, but the consideration of AS inside the supersonic solar wind would require a different approach because the statistics of test particles in the Monte Carlo calculations closer to the Sun would not be sufficient for comparison with IBEX observations.

ISN atom transport through the heliosphere is described by the Boltzmann transport equation as the collisional mean free paths are comparable with the sizes of heliospheric structures, and thus, the gas-dynamic approach is not applicable (Heerikhuisen et al. 2006). In our analysis, the collision term in the Boltzmann equation includes loss and gain terms related to elastic and charge exchange collisions, which need to account for AS. To solve the Boltzmann equation, we implement a Monte Carlo integration scheme (e.g., Malama 1991; Heerikhuisen et al. 2006). However, we make changes discussed below to account for AS in the elastic and charge exchange collisions.

We simulate trajectories of ISN atoms through the outer heliosheath, assuming flow velocities and temperatures of plasma obtained from the global heliosphere model (Zirnstein et al. 2016). We use the same solution of the model as in Swaczyna et al. (2023a) to allow comparisons of our current results with those obtained for the ISN helium. The boundary conditions of the global heliosphere model are listed in Appendix A. This model uses the charge exchange cross-section formula from Bzowski & Heerikhuisen (2020), where it does not account for the AS of atoms and ions. The results of test particle calculations are not reflected in the flows and temperatures. As such, the calculations are not self-consistent. However, while AS effects may affect the distribution functions of ISN atoms, Heerikhuisen et al. (2009) concluded that the AS related to charge exchange collisions does not significantly influence the global heliosphere structure or flows of neutral and charged components. Therefore, the higher-order effects should not invalidate the conclusions of this study.

In contrast to helium, charge exchange and elastic collisions between hydrogen atoms and protons are the two dominant types of collisions of hydrogen atoms in the outer heliosheath. Collisions with He^+ ions are an order of magnitude lower due to ∼2–3 times smaller cross section and ∼6 times lower density of He^+ ions than protons (Bzowski et al. 2019). Furthermore, we do not account for elastic collisions between hydrogen atoms because they would require a global heliosphere model that accounts for these collisions self-consistently. Nevertheless, these collisions do not transfer momentum between populations but lead to the internal thermalization of ISN hydrogen atoms. The relevant cross section for such a study can be found in Ovchinnikov et al. (2017). While a detailed study of this problem is beyond the scope of this paper, the frequency of these collisions is insufficient to fully thermalize the ISN hydrogen population in the outer heliosheath (in contrast to the distant ISM).

2.1. Numerical Method

The details of the numerical approach used in this study are presented in Swaczyna et al. (2021, 2023a). Below, we briefly summarize the most important steps. The Monte Carlo calculations start at the outer boundary, 500 au from the Sun, where we randomly select the initial state vectors of ISN hydrogen atoms from the pristine VLISM Maxwell distribution. The atoms are tracked until their distance from the Sun is less than 100 au (inner boundary) or until they cross the plane that contains the Sun and is perpendicular to the flow velocity vector of the pristine VLISM. During their journey between the outer and inner boundary, we neglect radiation pressure because, according to Kowalska-Leszczynska et al. (2022), the part of the solar Lyα line responsible for radiation pressure on ISN hydrogen atoms is almost fully absorbed beyond 100 au.

Along the tracked trajectory, we calculate probabilities of charge exchange and elastic collisions with protons as a product of the integral cross sections from (Schultz et al. 2016), the proton density from the global model, and the effective relative speed. The relative speed is calculated assuming Maxwell distribution of the plasma as in Ripken & Fahr (1983). For this calculation, we linearly interpolate the numerical cross section. These probabilities are used to randomly select whether a collision occurred within each step. The step size is defined so that the combined collision probability does not exceed 5% and the trajectory length within the step is less than 3 au.

If the collision occurs, we draw 10 proton velocities from the Maxwell distribution for the plasma bulk speed and temperature taken from the global model. The products of the integral cross sections and the relative speeds for the collisions with these protons are used as weights to select one of these protons as a colliding particle. This procedure is to account for the unequal collision probability with different parts of the distribution function. Swaczyna et al. (2021) verified that increasing the number of drawn collisions above 10 did not significantly change the results for collisions of helium atoms. Subsequently, for the collision energy of the selected pair, we randomly chose one of the two closest grid energies for which the differential cross sections are available (Schultz et al. 2016) using weights inversely proportional to the differences of the energy logarithms. Schultz et al. (2016) tabulated differential cross sections using 768 non-uniformly distributed scattering angles, providing a good representation of the variability with the scattering angle. The scattering angle is drawn from this set of angles based on the width of the angular bin and the differential cross section. The azimuthal angle about the initial particle speed is selected from a uniform distribution. We calculate the final velocity of the atom based on the initial velocity vectors for the pair of colliding particles and the angles.

The Monte Carlo calculations are repeated with and without accounting for the AS. While in the case without the AS, elastic collisions are irrelevant, charge exchange collisions are included, but the scattering angle is set to 0, i.e., newly created atoms have the same momentum as their parental protons. In both cases, we performed calculations for 5×10^7 initial state vectors at the outer boundary.

The charge exchange collisions between the heliopause and inner boundary may result in ENAs with energies substantially exceeding those of the primary and secondary neutrals. We remove these atoms from further analysis based on their velocity in the frame in which the x-axis is aligned with the inflow direction if $\max(|v_x - 25|, |v_y|, |v_z|) > 25$ km s^{-1}.

2.2. ISN Hydrogen at 100 au

We find the properties of atoms at the inner boundary as a function of their entrance position at 100 au from the Sun using the procedure described in Swaczyna et al. (2023a). First, we determine the density and bulk flow velocity of the primary and secondary ISN hydrogen populations as a function of their position at the inner boundary. In the next step, we characterize the 3D distribution functions using components parallel and perpendicular to the bulk flow velocity in the solar frame separately for each population. To characterize the distribution function, we combine the velocities of tracked atoms in the local bulk flow reference frame from all entry positions at 100 au. We visually inspected that the distribution functions in this frame do not strongly depend on the entry position (see Appendix B). Table 1 shows a summary of the properties of

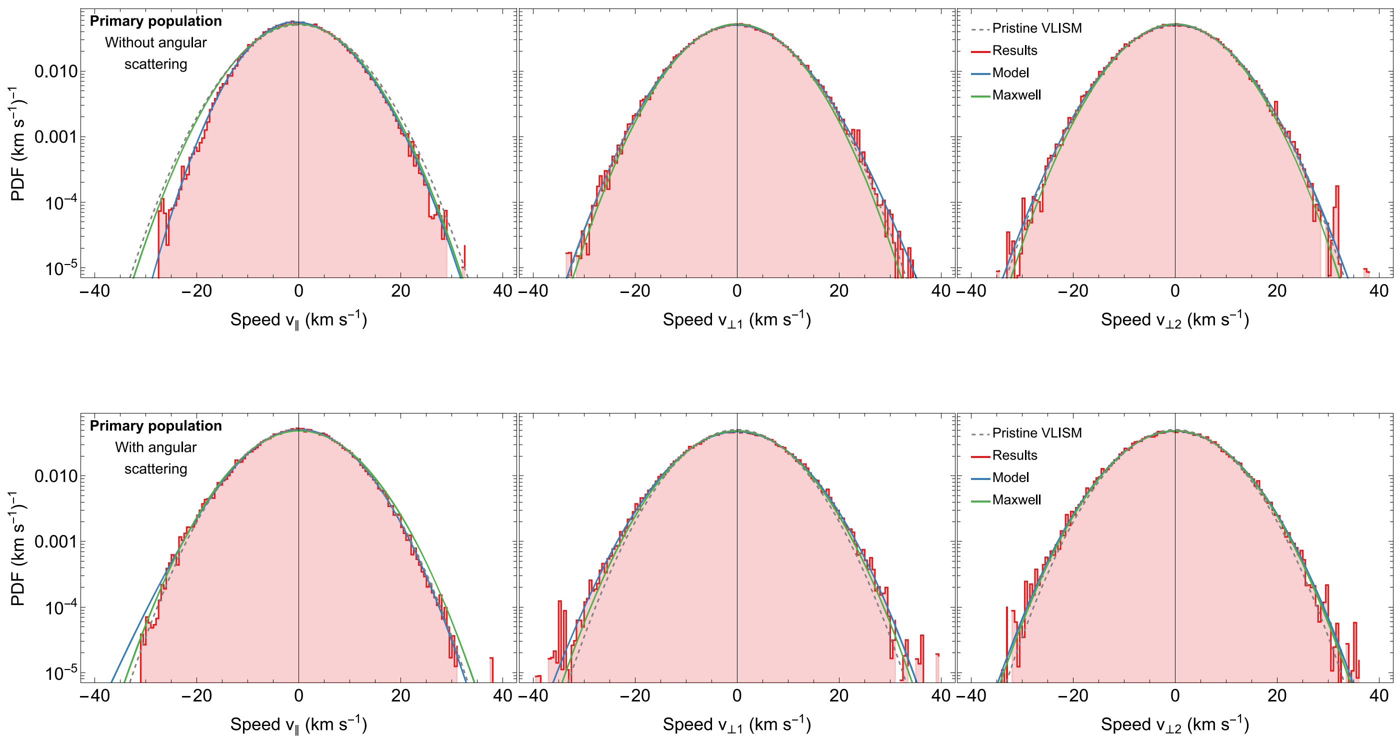

Figure 1. Combined normalized distribution functions of the primary population of ISN H from all entry points at 100 au. Panels from left to right show the parallel and two perpendicular components. The bulk speed is subtracted from the parallel component, and positive parallel speeds correspond to atoms moving faster than the bulk flow toward the Sun. The top and bottom rows present the results obtained without and with accounting for the AS in collisions. The red histogram presents the results of the Monte Carlo simulations, and the blue and green lines show the analytic model derived in Appendix B, and the Maxwell approximation (Table 1), respectively. The shape of the Maxwell distribution in the pristine VLISM ($T = 7500$ K) is shown with a dashed gray line.

Table 1
Properties of ISN Hydrogen Populations at 100 au

Population	AS	n/n_∞	v (km s^{-1})	α (deg)	$T_\parallel(K)$	$T_\perp(K)$
Model VLISM	⋯	1	25.4	0	7500	7500
Primary	With	0.224	26.5	+1.3	7540	8440
	Without	0.229	27.8	+0.5	6160	7540
Secondary	With	0.521	16.8	+8.8	10130	11020
	Without	0.508	16.6	+7.8	9860	11050

these populations. The table shows the results obtained with and without including the AS. In both cases, the charge exchange collisions are accounted for, but for the calculations without AS, the speed of the newly neutralized atoms is adopted from the velocity of the parent proton.

The table shows the relative density of each population compared to the density of ISN hydrogen far from the Sun (n/n_∞), the bulk speed of atoms along the inflow direction (v), the deflection angle from the flow direction far from the Sun (α), and temperature of the distribution in the direction parallel ($T_\parallel$) and perpendicular ($T_\perp$) to the local bulk flow direction at the entry point at 100 au. The temperatures provided here are calculated from the mean thermal speed. Figures 1 and 2 present the distribution functions of the parallel and perpendicular velocity components in the frame oriented along the bulk flow at 100 au. The figure compares the histograms obtained from the Monte Carlo simulations, the approximation using the Maxwell distributions with temperatures provided in Table 1, and the analytic distribution functions derived in Appendix B.

Unlike ISN helium (Swaczyna et al. 2023a), the primary population of ISN H in each direction can be relatively well represented by Maxwell distribution with temperatures presented in Table 1 (see Figure 1). However, the secondary population requires a superposition of four Maxwellian populations to capture the complexity of the parallel component and asymmetric kappa distributions (Swaczyna et al. 2021) to model the perpendicular components (see Appendix B).

The modeling results without the AS show that the primary population is apparently *accelerated* before it reaches 100 au. While we include gravity, it is responsible for a speed increase by only $\sim$0.4 km s^{-1} compared to the pristine VLISM. The remaining difference is due to the charge exchange process more effectively removing primary atoms that are moving slower relative to the Sun because they also move slower relative to the decelerated outer heliosheath plasma and the cross section increases for lower collision speeds (Izmodenov et al. 2001; Heerikhuisen et al. 2016; Bzowski & Heerikhuisen 2020). The same effect causes a reduction of the parallel temperature of this population. The preferential removal of atoms by charge exchange collisions also deflects the bulk velocity by $\sim+0.^\circ5$ away from the flow direction within the B–V plane defined by the interstellar flow velocity and

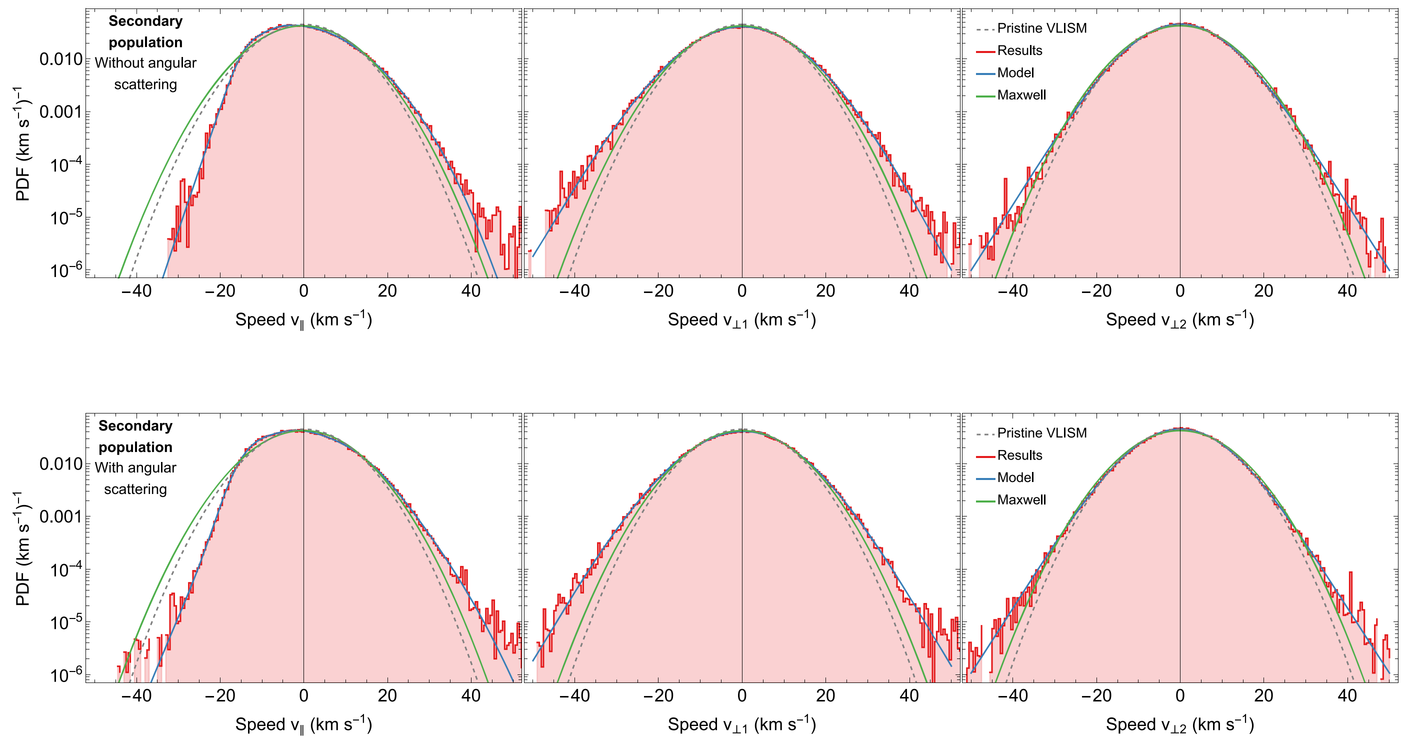

Figure 2. As in Figure 1, but for the secondary population.

magnetic field direction. The positive value of this angle means that the apparent inflow direction is closer to the interstellar magnetic field direction. The inclusion of the AS slows down the population by $\sim$1.3 km s^{-1}, increases the deflection by $\sim$0$^\circ\!\!.$8, and increases temperature by $\sim$1100–1300 K.

In both cases, the secondary population obtained in our analysis is slower, more deflected within the *B*–*V* plane, and warmer than the primary population, as is expected from the population forming the Hydrogen wall (Baranov & Malama 1993; Izmodenov et al. 2005). However, the AS effects are much weaker than the estimate for the ISN helium populations; the speed increases by just $\sim$0.2 km s^{-1}, the deflection angle increases by $\sim$1°, and the temperature remains almost the same. These changes differ from the conclusions of Swaczyna et al. (2019), who showed that the secondary population obtained from the charge exchange of neutral hydrogen atom and proton populations moving with respect to each other with a relative bulk speed of $\sim$20 km s^{-1} resulted in a secondary population moving faster relative to the Sun by $\sim$2 km s^{-1} if the AS is accounted for. They also predicted that the population would be substantially warmer. However, the analysis by Swaczyna et al. (2019) considered idealized charge exchange collision of two Maxwell populations, neglecting any subsequent collisions of secondary atoms in the outer heliosheath. Our current analysis shows that the atoms that undergo one charge exchange collision are subsequently more likely to undergo additional collisions, including another charge exchange, than the primary atoms. Therefore, subsequent collisions reduce the AS effect because the typical relative collision speed between a secondary atom and proton is much lower.

The primary population is composed of atoms that are not subject to charge exchange collision between the outer and inner boundaries. On the other hand, the secondary population is formed by those created through charge exchange in this region. The distance of the outer boundary (500 au) is adopted so that the plasma and neutral flows beyond this distance are close to their pristine conditions. Nevertheless, the secondary atoms from charge exchange collisions near the outer boundary have properties close to the primary atoms and could also be classified as such. As we discussed in Swaczyna et al. (2023a), this would not impact the combined population as long as we consider the sum of these two populations, but any comparisons of the primary and secondary population properties need to account for this somewhat arbitrary separation of the two populations. The significance of the distance of the inner boundary is less important as long as it is located within the heliopause, so we can assume that the accumulation of the secondary population ceased.

3. Modeling ISN H inside 100 au Boundary

The analytical full integration model (aFINM) is an attempt to integrate the analytic relations based on the classical hot model adapted by Lee et al. (2012) to the IBEX observation strategies. These observation strategies are introduced to our simulations through three numerical integrations over the instrument response function and spin sector to calculate ISN count rates observed by IBEX-Lo. This model has been previously used to characterize the ISN H (Schwadron et al. 2013; Rahmanifard et al. 2019), ISN He (Schwadron et al. 2015), and ISN O (Schwadron et al. 2016) flow. In these studies, as in Lee et al. (2012, 2015) a drifting Maxwellian distribution is used for the primary population of ISN atoms at infinity:

$$f_i = n_i(2\pi k_B T_i/m)^{-3/2} \times \exp(-|\vec{V}_\infty - \vec{V}_i|^2(2k_B T_i/m)^{-1}), \quad (1)$$

where $\vec{V}_\infty$ is the velocity for an ISN atom with a given energy at a specific observation geometry traced back to the termination shock (which we assumed to be located at infinity in aFINM2019). n_i, T_i, and $\vec{V}_i$ are the density, temperature, and bulk flow velocity for the primary ISN atoms. In Rahmanifard et al. (2019), we further considered a secondary population for ISN H atoms with a drifting Maxwellian as described by Equation (1) so that the distribution function includes both primary and secondary populations

$$f = \sum_{i=\mathrm{prim,sec}} f_i, \tag{2}$$

where we adopted parameters associated with primary and secondary populations from previous studies (Bzowski et al. 2008; Kubiak et al. 2016, etc.).

In this study, however, we consider the transport of ISN atoms through the outer heliosheath based on the global heliosphere model (Zirnstein et al. 2016). As described in Section 2, the transport of ISN atoms in the heliosheath is considered between 500 au and an inner boundary at 100 au, where aFINM takes over the resulting distribution function. This 3D distribution function is a combination of ISN primary and secondary populations. Therefore, we have modified the aFINM model to accept distribution functions that are a function of the position relative to the Sun, as well as the velocity. We no longer use a drifting Maxwellian as the distribution function for the primary and secondary populations at infinity. Instead, we use the results from Section 2.2 (the red histogram from Figures 1 and 2). Hence, we do not use ISN parameters from previous studies as we did for aFINM2019.

To make this change, we used a different set of equations for the trajectory of ISN atoms, as shown in Appendix A of Swaczyna et al. (2023a). We further made two modifications to account for the radiation pressure: first, the standard gravitational parameter of the Sun was replaced with an effective gravitational parameter $\alpha = (1 - \mu)GM_\odot$, where $GM_\odot = 1.3271244 \times 10^{22}$ m^3 s^2, and the energy of the atom is $E = mV^2/2 - \alpha/r$, where $\vec{r}$ is the position vector and r is its magnitude; additionally, the eccentricity sign adopted in their equations was changed for a repulsive force, i.e., when $\mu > 1$. The geometry of IBEX observation used in aFINM2019 is provided in Lee et al. (2012) and the modifications we used for the current version of aFINM are provided in Appendix A of Swaczyna et al. (2023a).

With the above changes, we calculate the position and velocity vectors at the 100 au inner boundary for a given energy at a specific IBEX observation geometry. Based on these values we find the distribution function value at the inner boundary, which is further multiplied by a survival probability that is calculated based on photoionization and charge exchange probabilities to obtain the distribution function at 1 au. We implement values averaged over the last seven Carrington rotations of the atoms' trajectory to calculate their photoionization and charge exchange rates. During this time the ionization rates are above ∼10% of their values at 1 au (see Sokółet al. 2013; Sokół& Bzowski 2014; Rahmanifard et al. 2019; Sokół et al. 2020, for further details). We use the Lindsay & Stebbings (2005) formula for the charge exchange cross section and solar wind speed and density associated with the heliolatitude of the incoming atoms from Sokół et al. (2020). Photoionization rates are also obtained from a model described in Sokół et al. (2020). We then calculate the flux of ISN H atoms and integrate over the response function of the instrument, including energy and collimator response functions to find the observed count rates at a specific time and specific spin angle. We further integrate over a full spin bin and a good times list of an orbit to provide the observed count rates associated with that orbit and spin bin.

3.1. Numerical Method

Our main purpose here is to determine how considering the AS caused by charge exchange and elastic collisions in the heliosheath affects the results we obtained from Rahmanifard et al. (2019). Therefore, we concentrate on the longitudinal shift in the peak of the ISN H signal and find an effective radiation parameter that matches this shift for each year. The longitude, in this paper, represents the ecliptic longitude of IBEX, from the fall equinox, at the time of observation.

As detailed in Rahmanifard et al. (2019), we found an effective value for the radiation parameter (μ_{eff}) with the best agreement between the observed and model-predicted λ_{peak} (the longitude at which the ISN H signal peaks). Therefore, we do not incorporate any physical model for the parameter μ and its dependence on time, radial speed, or heliolatitude.

To find the observed λ_{peak}, we first ran a χ^2 minimization analysis to fit a Gaussian to the observed ISN H signal each year. Our focus was on IBEX-Lo spin sectors 14 and 15, which correspond to 6° bins with their centers located at 84° and 90° from the north ecliptic pole (NEP). We used these two spin bins because they are closest to the latitudinal peak of the signal and provide higher statistics. Furthermore, we used the signal observed in E-Step 1 because it is the only energy channel where we can observe ISN H throughout almost the entire solar cycle. While the ISN H signal is present in E-Step 2 for the first years of IBEX observations, count rates in E-Step 2 are statistically zero for all the remaining years. This decrease is partly due to moving toward a solar maximum, and partly due to lowering the post-acceleration (PAC) voltage from 16 to 7 kV in the summer of 2012.

While the focus of this study is on the longitudinal shift of the signal peak, strong variations of the intensity of the signal with solar activity affect the analysis. Moving toward a solar maximum caused the relatively noticeable signal associated with the years 2009–2011 to decrease to values close to the background level in 2012. The signal became undetectable for the years 2013–2015 mostly due to extensive ionization and radiation pressure during solar maximum. Also, the reduction in the PAC voltage lowered the statistics by half. We further missed the signal for the year 2016 due to a different stepping scheme. Therefore, the focus of Rahmanifard et al. (2019) and this study is on the years 2009–2012 and 2017–2018. We further added 2013 and 2014, without running a χ^2 analysis since there are too few data points to run one. Instead, we simply used the highest data point as the peak of the signal for these two years.

We then performed a set of χ^2 analyses to fit a Gaussian to our model-predicted count rates to find values for λ_{peak} from our model for different values of the radiation pressure parameter. Running this analysis iteratively, we found μ values that matched λ_{peak} from the observations. The effective μ values (μ_{eff}) we obtained in this way are empirical.

Using a Gaussian fit to find λ_{peak} for the observed and predicted ISN H signal is a reasonable method. Figure 3, which we have adopted from Figure 4 in Rahmanifard et al. (2019)

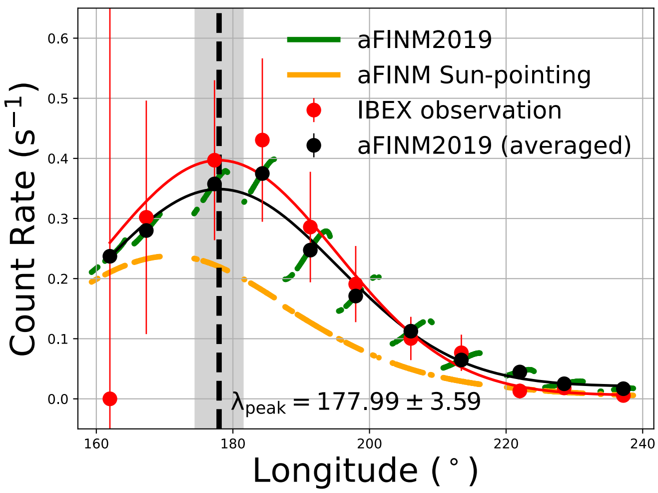

Figure 3. Model predictions based on aFINM2019 compared to IBEX-Lo observations of ISN H for the year 2011 (E-Step 1, spin bin 14) adopted from Rahmanifard et al. (2019). The green and orange lines show model predictions for actual IBEX observations and Sun-pointing Earth location and reference frame. The black line is the Gaussian fit to model predictions averaged over the times when IBEX data is available (black data points) and the red line is the Gaussian fit to IBEX data (red data points). The dashed black line shows the peak longitude of the ISN H signal and the gray area shows the uncertainty region.

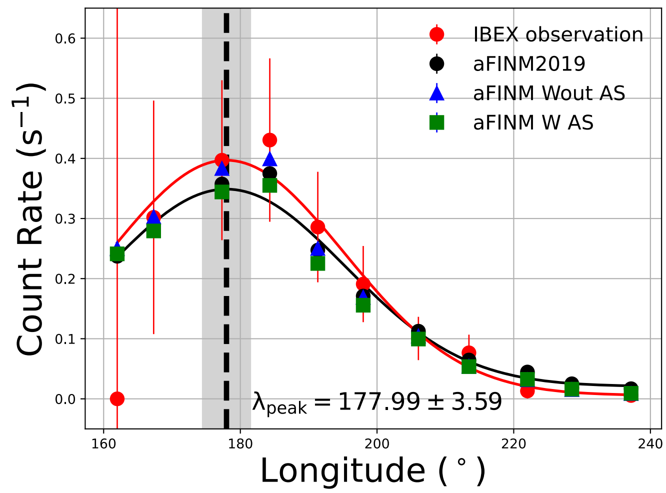

Figure 4. Model predictions based on aFINM2019 (black circles) and modified aFINM for the two cases with (green squares) and without (blue triangles) AS compared to IBEX-Lo observations (red circles) of ISN H for the year 2011 (E-Step 1, spin bin 14). The black line is the Gaussian fit to aFINM2019 and the red line is the Gaussian fit to IBEX data. The dashed black line shows the peak longitude of the ISN H signal and the gray area shows the uncertainty region.

shows aFINM2019 predictions for IBEX observations in spin sector 14 in the 2011 ISN H season. The green line shows aFINM2019 predictions for IBEX observations throughout each orbit using the exact spacecraft's position, velocity, and spin axis. The orange line, on the other hand, represents the Earth-located aFINM2019 predictions in the Earth reference frame with the spin axis of the instrument Sun-pointing at all times. The black circles show the predicted count rates (the green line) averaged over the observation times and the red circles with error bars show the the observed count rates. The black (red) line presents a Gaussian fit to the black (red) circles. Comparing the green and orange lines demonstrates the effect of the spacecraft motion and the field-of-view drifts relative to the ideal Sun-pointing spin axis creating the sawtooth patterns. In addition to these effects, differently distributed observation times for each orbit lead to a deviation from the Gaussian fit, especially for orbit 118 (the fourth orbit from the left) in Figure 3. Despite such deviations, using a Gaussian fit in our analysis is reasonable since we include these effects in our model and use the same techniques to find the peak for the observed and predicted signal. It is important to note that the absolute location of λ_{peak} does not play a role in our analysis. Therefore, as can be seen in Figures 3 and 4, we use the peak of the Gaussian fit (dashed black line with gray uncertainty region) rather than the maximum measured count rate.

Figure 4 shows our results for the year 2011 in sector 14 as an example to compare our aFINM2019 results with the current version of the code in which we consider charge exchange and elastic collisions in the heliosheath. All aFINM simulation results presented in Figure 4 are based on μ_{eff} as obtained in our previous study for the year 2011 ($\mu_{eff} = 1.10424$). We present the observed count rates for each orbit as red circles with error bars and the predicted aFINM2019 rates as black circles. We further include our modified version of aFINM, with (green squares) and without (blue triangles) AS from charge exchange and elastic collisions.

3.2. ISN Hydrogen at 1 au

The main difference between aFINM2019 and aFINM without AS in this figure is the selective charge exchange in the outer heliosheath (as detailed in Section 2 and Appendix B). Additionally, using the inner boundary at 100 au rather than using pristine parameters at infinity for the primary population leads to slightly different trajectories inside the heliosphere as described earlier. As discussed in Section 2, the selective charge exchange leads to a faster and cooler primary population. The results, as can be seen in Figure 4, do not show a significant shift in the peak location between aFINM2019 and the modified version of aFINM without AS, except for a small relative increase close to the peak compared to the flanks of the signal. This difference may arise from the fact that in the new version, the speed difference between the primary population (dominant in the peak) and the secondaries (dominant in the flanks) is even more pronounced than in aFINM2019.

The green squares in Figure 4 account for the AS both in the charge exchange and elastic collisions. The selective charge exchange of the primary H population in the outer heliosheath is present for this case (with AS) as well. However, as explained in Section 2, accounting for the AS in the charge exchange and elastic collisions slows down the primary ISN H significantly; thus, the predicted signal for this case shows lower count rates close to the peak.

We performed this analysis for the years 2009–2018 (spin bins 14 and 15), excluding 2015–2016, with the new version of the code, for the two cases with and without AS. We present the results in Figures 5 (spin bin 14) and 6 (spin bin 15). We see the same pattern as in aFINM2019, with slight variations in the μ values. Despite these small variations, the same trend still persists. Black, red, and green circles with error bars, respectively, represent aFINM2019, aFINM without AS, and aFINM with AS. We slightly shifted the data points for aFINM without AS and aFINM with AS in time to enhance their visibility. The predicted μ values in the second panels of Figures 5 and 6 increased for the years 2009–2012 in accordance with an increase in solar activity. Using the

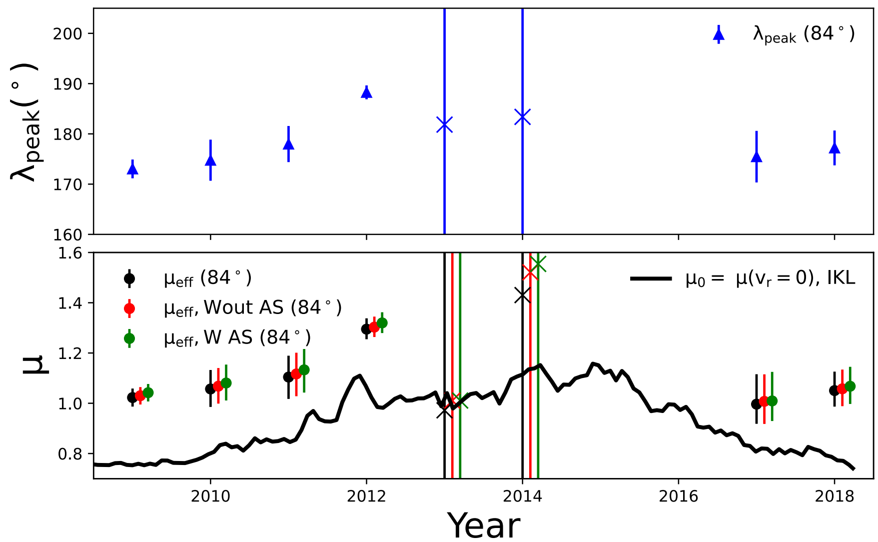

Figure 5. ISN H flow peak longitude based on IBEX observations at spin bin 14 (84° from the NEP). Blue triangles with error bars are found by fitting a Gaussian function to the ISN H signal for the years 2009–2012 and 2017–2018. Blue x marks used for the years 2013 and 2014 are obtained based on the highest observed data points. Bottom panel: $\mu_{\rm eff}$ obtained based on our analysis for aFINM2019 (black), modified aFINM without AS (red), and with AS (green) circles with error bars for the spin bin 14 data. The black line represents μ_0 based on Kowalska-Leszczynska et al. (2018b; IKL).

maximum count rate in 2013 and 2014 as the peak of the distribution indicates a further increase in the predicted $\mu_{\rm eff}$ as expected. Finally in 2017–2018 on the way toward solar minimum, a decrease is evident. These variations in $\mu_{\rm eff}$ are in accordance with previous findings (Rahmanifard et al. 2019).

We further see that the estimated $\lambda_{\rm peak}$, and thus, the obtained $\mu_{\rm eff}$ from our χ^2 analysis, are generally smaller for spin bin 15 (in Figure 6) than for spin bin 14 (Figure 5). Since this analysis only includes these two spin bins (due to low statistics in other spin bins), we cannot conclude on the latitudinal variations in the radiation parameter.

The black line in the second panels of Figures 5 and 6 shows $\mu_0 = \mu(v_{\rm r} = 0)$, where $v_{\rm r}$ is the radial velocity of ISN H atoms (Kowalska-Leszczynska et al. 2018b). μ_0 from Kowalska-Leszczynska et al. (2018b) clearly demonstrates the same trend as $\mu_{\rm eff}$ derived from the IBEX observations in this study (black, red, and green circles with error bars), despite a quantitative difference. It is important to note that $\mu_{\rm eff}$ is an empirical μ, which may best be represented by μ values for a weighted average of $v_{\rm r}$ in the last months of the ISN H atoms' journey toward the Sun. In Rahmanifard et al. (2019), we showed that while this $\bar{v}_{\rm r}$ in the last 6 months of the ISN H atoms journey is ~ -18.3 km s^{-1}, $\mu_{\rm eff}$ based on aFINM2019 is equivalent to $\mu(v_{\rm r} = -35 \text{ km s}^{-1})$. Furthermore, considering the shape of the Lyα profile, the ~ -18.3 km s^{-1} radial speed falls into the flat part of the profile so that μ_0 can be a good approximation for the $\mu_{\rm eff}$. Therefore, we expect the quantitative difference between the μ_0 and $\mu_{\rm eff}$ in Figures 5 and 6 to be at least partially associated with the absolute calibration of Lyα line profiles.

A linear correlation has been reported between the total Lyα irradiance and μ_0 (Lemaire et al. 2015). We illustrate this correlation in Figure 7 with a blue line and blue shaded area for the uncertainty region; $\mu_0 = (0.35 \pm 0.01) \times 10^{-11} \times I_{\rm t} - (0.46 \pm 0.005)$. To find μ_0 that best describes what ISN H atoms have experienced in each season (in analogy to $\mu_{\rm eff}$), we use the total Lyα irradiance averaged over two Carrington cycles before the start of each ISN H season. This approach is based on a discussion in Rahmanifard et al. (2019), where we showed the net force acting on ISN H atoms remains negligible until the last few au of their trajectory or the last two months of their journey toward the Sun. We compare this correlation (blue line) with a correlation between $\mu_{\rm eff}$ (aFINM2019, the two cases with and without AS) and the total irradiance. The correlations for these three cases are not significantly different (shown in black, red, and green for the aFINM2019, without AS and with AS), as expected:

$$\mu_{\rm eff}^{\rm aFINM2019} = (0.27 \pm 0.03) \times 10^{-11} I_{\rm t} + (0.03 \pm 0.10), \quad (3)$$

$$\mu_{\rm eff}^{\rm Wout\ AS} = (0.28 \pm 0.03) \times 10^{-11} I_{\rm t} + (0.01 \pm 0.11), \quad (4)$$

$$\mu_{\rm eff}^{\rm W\ AS} = (0.29 \pm 0.03) \times 10^{-11} I_{\rm t} - (0.005 \pm 0.127). \quad (5)$$

4. Summary and Discussion

In this paper, we followed the methodology developed to model collisions of ISN helium atoms by Swaczyna et al. (2021, 2023a). We used Monte Carlo simulations of test particle trajectories to simulate the transport of ISN atoms through the outer heliosheath accounting for the AS associated with the AS of atoms and ions starting at 500 au with a Maxwellian distribution. We considered charge exchange and elastic collisions between ISN H atoms and protons for which we investigated two cases where these collisions occur with and without AS all the way to 100 au. We did not include collisions between hydrogen atoms. These collisions lead to the thermalization of ISN hydrogen atoms and do not transfer momentum between populations. Additionally, these collisions may transfer momentum between the H atoms and modify their distribution function. However, this effect cannot be studied under the test particle approach implemented here. Therefore, it needs to be addressed in the future.

Using this method, as described in more detail in Section 2 (also see Swaczyna et al. 2023a), we found the ISN H atoms distribution at 100 au as a function of their entrance position and their velocity. We approximated this distribution function by Maxwellian functions separately for the primary and secondary ISN atoms. The parameters associated with these

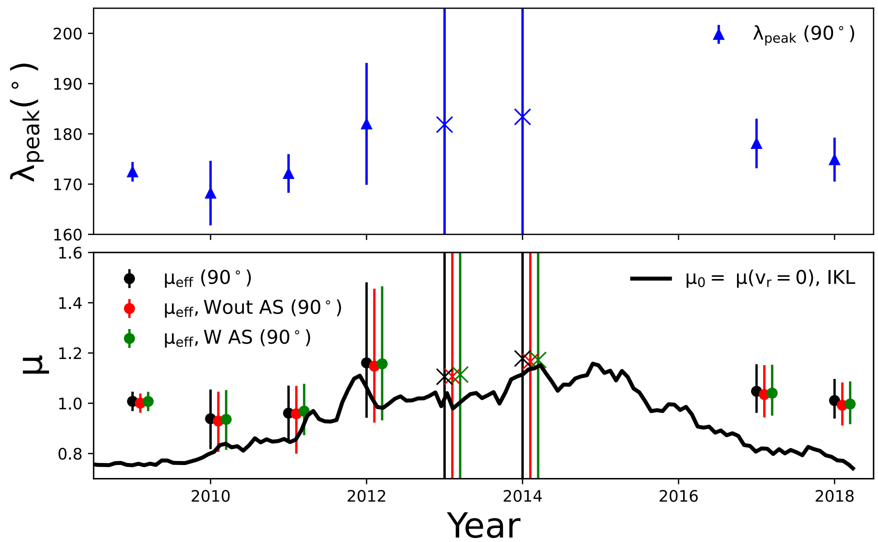

Figure 6. As in Figure 5 but for spin bin 15 (90° from the NEP).

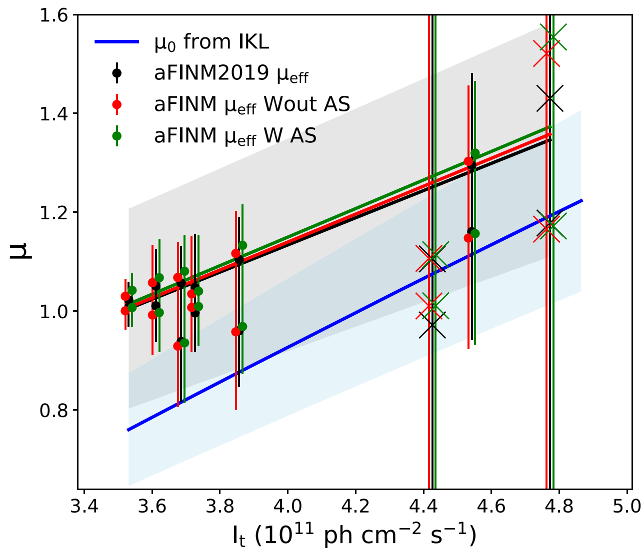

Figure 7. The $\mu_{\rm eff}$ obtained from our analysis for aFINM2019 (black), modified aFINM without AS (red), and with AS (green) circles with error bars for spin bins 14 and 15 data vs. total irradiance. The linear correlation between μ_0 from (Kowalska-Leszczynska et al. 2018b; IKL) and total irradiance is shown by the blue line with light blue the uncertainty region. The black, red, and green lines represent the linear fit to black, red, and green data points respectively. The data points presented by x marks are not included in the linear fit as they are associated with the years 2013 and 2014 where a χ^2 analysis is not possible. The gray uncertainty region is associated with aFINM2019 (black line).

Maxwellian functions are presented in Table 1. These parameters show that considering AS decelerates and heats primary ISN H, and thus, reduces the effect of selective charge exchange in the outer heliosheath. Secondary ISN H atoms, on the other hand, are not significantly affected by AS. We further provide a more rigorous approximation of the distribution function at 100 au in the form of analytic models separately calculated for each component in Appendix B. The two approximations (Maxwellian and analytic model) are presented to show the effect of AS on the distribution function of ISN H atoms in the inner boundary.

Based on our calculated distribution function at 100 au, we then used a modified version of the aFINM model (Section 3 and Swaczyna et al. 2023a) to obtain the ISN H count rates observed in the lowest energy bin of IBEX-Lo. We performed an analysis of the observed ISN H signal in the two spin bins closest to the latitudinal peak of the signal (bins 14 and 15, corresponding to 84° and 90° from the NEP).

To investigate the ISN H signal and its evolution over the solar cycle, besides the variation in the intensity of the ISN H signal, the longitudinal shift of the ISN H signal over different phases of solar activity is of key interest. These effects were first reported by Saul et al. (2012, 2013). However, due to a discrepancy in the ratio of H counts in the two lowest E-Steps between models and IBEX observations, only a few studies have addressed variations in the intensity of ISN H signal (Schwadron et al. 2013; Katushkina et al. 2015) for limited IBEX observations. In Rahmanifard et al. (2019), we used an almost entire solar cycle worth of data (Galli et al. 2019) to investigate the effect of the radiation parameter on the longitudinal shift of the ISN H signal. Katushkina et al. (2021) further used a combination of these two effects to investigate the radiation parameter and variations of ISN H signal through different phases of solar activity.

In this paper, we used the methodology introduced in Rahmanifard et al. (2019) to find an effective radiation parameter using the same ISN H seasons. We investigated the effect of the radiation parameter on the longitudinal shift of ISN H signal for the cases where we used aFINM2019 and modified aFINM results with and without AS. We showed the two cases with and without AS demonstrate the longitudinal shift in accordance with variations in solar activity, as does aFINM2019. Additionally, the average value for the predicted $\overline{\mu}_{\rm eff}$, including $\mu_{\rm eff}$ values for both spin bins 14 and 15, over the years included in this analysis are not significantly different.

$$\overline{\mu}_{\rm eff}^{\rm aFINM2019} = 1.074 \pm 0.038, \tag{6}$$

$$\overline{\mu}_{\rm eff}^{\rm Wout\ AS} = 1.079 \pm 0.039, \tag{7}$$

$$\overline{\mu}_{\rm eff}^{\rm W\ AS} = 1.087 \pm 0.040. \tag{8}$$

Compared to $\overline{\mu}_0 = 0.84 \pm 0.067$, averaged over the same time span, based on Kowalska-Leszczynska et al. (2018b), the derived $\overline{\mu}_{\rm eff}$ values (Equations (6)–(8)) present a ∼22%–23% increase, with the case considering AS slightly larger than the case without considering the AS. Because the ∼22%–23% larger $\overline{\mu}_{\rm eff}$ value than $\overline{\mu}_0$ for all the three cases investigated in this paper is in line with our previous findings from Rahmanifard et al. (2019), these values confirm that considering charge exchange and elastic collisions and their associated AS in the outer heliosheath does not introduce a significant difference in the position of the ISN H peak. Furthermore, accounting for AS in elastic collisions and charge exchange does not resolve the quantitative difference between $\overline{\mu}_0$ and $\overline{\mu}_{\rm eff}$.

The IMAP-Lo instrument, part of the upcoming IMAP mission (Interstellar Mapping and Acceleration Probe, McComas et al. 2018) is expected to provide higher statistics and a broader and better-understood instrument response to ISN H atoms, which will eventually lead to better possibilities to investigate the ISN H signal. Future IMAP-Lo observations with their improved statistics, the better-defined instrument response function, and the wider range of observation season and thus vantage points thanks to the pivot platform will improve our understanding of ISN H and its fate in the heliosphere (Sokół et al. 2019). We hope that extending this kind of analysis to investigate the ISN H signal observed at different vantage points through longer observation seasons provided by IMAP-Lo will improve our understanding of the ISN H filtration and interaction in the heliospheric boundaries, and thus, will address the ∼22%–23% discrepancy between the ISN H-derived and solar EUV-derived μ parameter.

Acknowledgments

This work was supported by the National Aeronautics and Space Administration under grant No. 80NSSC20K0781 issued through the Outer Heliosphere Guest Investigators Program. A.G. thanks the Swiss National Science Foundation for financial support. This work was also partially funded by the IBEX mission as part of NASA's Explorer Program (80NSSC18K0237) and IMAP mission as a part of NASA's Solar Terrestrial Probes (STP) Program (80GSFC19C0027). J.M.S. is supported by the IBEX mission grant 80NSSC20K0719. Research at SwRI was funded by a subcontract from Princeton University. P.S. contributed to the original submission while working at Princeton University, but he contributed to the revision at the Space Research Center PAS within a project co-financed by the National Agency for Academic Exchange, within the Polish Returns Program (BPN/PPO/2022/1/00017), with a research component funded by the National Science Center, Poland (2023/02/1/ST9/00004). F.R., P.S., A.G., and J.H. acknowledge the discussion within the framework of ISSI International Team #541 Distribution of Interstellar Neutral Hydrogen in the Sun's Neighborhood.

Appendix A
Boundary Conditions of the Global Heliosphere Model

This appendix briefly describes the adopted boundary conditions of the global heliosphere model far from the Sun. A more detailed discussion can be found in Swaczyna et al. (2023a, 2023c). The inner boundary conditions are selected based on the average calculated from the OMNI collection for four solar cycles before the maximum of solar cycle 24. The plasma density is assumed 8.3 nuc cm^{-3}, including 4% of α-particles, the bulk velocity is 441.5 km s^{-1}, the temperature is 51,000 K, and the radial component of the magnetic field is 37.5 μG. The model does not include helium ions as a separate fluid, but instead, the effective densities included in the charge exchange terms are scaled down to mimic their presence. The outer boundary conditions in the VLISM have been adopted as follows: inflow direction in the ecliptic coordinates—(255°.7, 5°.1), bulk speed—25.4 km s^{-1}, temperature—7500 K, magnetic field strength—2.93 μG, magnetic field direction in the ecliptic coordinates—(227°.28, 34°.62), plasma density—0.0856 nuc cm^{-3}, neutral hydrogen density—0.11 cm^{-3}.

Appendix B
Analytic Model of the ISN Hydrogen Distribution Function at 100 au from the Sun

The transport of ISN hydrogen atoms through the outer heliosheath is calculated using the Cartesian coordinate system in which the pristine VLISM inflow direction coincides with the x-axis, the pristine interstellar magnetic field direction is within the xy-plane, and the z-axis completes the right-handed coordinate system. Because of the limited statistics achievable in the Monte Carlo simulations, the distribution function reconstructed from the distribution of the velocity vectors at various entrance positions at 100 au from the Sun is limited. To provide a smooth approximation of the distribution function, we employ the two-step approach described in detail by Swaczyna et al. (2023a).

In the first step, we calculate each population's density and bulk velocity at the inner boundary relative to the density in the pristine VLISM as a function of the entry position. We define 20 × 20 au square cells in the yz-plane centered at ±10, ± 30, …, ± 90 au in the y and z directions. We divide the 100 au half-sphere into segments that coincide with these cells when projected onto the yz-plane. We select trajectories that crossed the 100 au sphere within each segment. Subsequently, we calculate the density and bulk velocity from this subset. The obtained densities and bulk velocities have significant numerical uncertainties. To focus on the main variability as a function of the entry position, we fit a smooth function of y and z for the density and each velocity component, separately for the primary and secondary populations. We use a multivariate polynomial up to the degree of 4 to parameterize this function:

$$f(y, z) = \sum_{i=0}^{4}\sum_{j=0}^{4-i} a_{i,j}\left(\frac{y}{100\text{au}}\right)^{i}\left(\frac{z}{100\text{au}}\right)^{j}. \tag{B1}$$

In the most general form, this formula has 15 coefficients. However, because we expect a symmetry with respect to the B–V plane (i.e., xy-plane), the density and x- and y-components of the bulk velocity must fulfill the following condition: $f(y, -z) = f(y, z)$, which means that the coefficient $a_{i,j}$ for $j = 1$, or 3, must be 0. On the other hand, for the z-component of the velocity, the function must satisfy $f(y, -z) = -f(y, z)$, which means that $a_{i,j}$ for j=0, 2, or 4 must be 0, which reduces the number of nonzero coefficients in each case. Unlike Swaczyna et al. (2023a), we do not separate the bulk velocity changes due to solar gravity. Table 2 presents the found coefficients for each population's density and bulk velocity.

In the second step, we find an analytic distribution function at 100 au. For each entry position, we define a rotation matrix that transforms the local bulk velocity estimated from

Table 2
Polynomial Coefficients for Densities and Velocities of the ISN Hydrogen Populations

Population	Quantity (Unit)	AS	Polynomial Coefficients								
			$a_{0,0}$	$a_{0,2}$	$a_{0,4}$	$a_{1,0}$	$a_{1,2}$	$a_{2,0}$	$a_{2,2}$	$a_{3,0}$	$a_{4,0}$
Primary	$n_{\rm pri}/n_\infty$ (1)	With	0.224	−0.028	0.024	0.005	0.016	−0.003	0.007	0.006	−0.004
Primary	$n_{\rm pri}/n_\infty$ (1)	Without	0.229	0.016	−0.034	0.006	0.005	0.009	−0.012	0.007	−0.023
Secondary	$n_{\rm sec}/n_\infty$ (1)	With	0.521	−0.071	−0.025	−0.044	0.027	−0.022	−0.091	0.041	−0.087
Secondary	$n_{\rm sec}/n_\infty$ (1)	Without	0.508	−0.044	−0.071	−0.001	−0.014	−0.047	−0.056	−0.022	−0.054
Primary	$v_{\rm pri,x}$ (km s^{-1})	With	26.46	1.04	−0.73	−0.24	0.06	1.33	−1.73	0.41	−1.24
Primary	$v_{\rm pri,x}$ (km s^{-1})	Without	27.76	0.27	−0.45	−0.07	−0.29	−0.07	0.19	0.13	−0.24
Secondary	$v_{\rm sec,x}$ (km s^{-1})	With	16.63	1.73	0.19	0.15	−0.78	1.41	−0.18	−0.29	0.08
Secondary	$v_{\rm sec,x}$ (km s^{-1})	Without	16.48	1.63	0.44	−0.72	0.39	2.07	−1.19	0.64	−0.47
Primary	$v_{\rm pri,y}$ (km s^{-1})	With	−0.59	0.21	−0.34	−0.40	−0.41	−0.08	0.66	−0.18	0.22
Primary	$v_{\rm pri,y}$ (km s^{-1})	Without	−0.22	−0.78	0.96	−0.40	−0.45	−0.15	0.34	−0.79	0.13
Secondary	$v_{\rm sec,y}$ (km s^{-1})	With	−2.59	1.70	−1.10	1.13	−1.54	−0.24	−0.27	−1.30	1.18
Secondary	$v_{\rm sec,y}$ (km s^{-1})	Without	−2.25	−0.16	0.75	0.77	−0.89	0.93	−0.47	−0.91	−0.82
			$a_{0,1}$	$a_{0,3}$	$a_{1,1}$	$a_{1,3}$	$a_{2,1}$	$a_{3,1}$			
Primary	$v_{\rm pri,z}$ (km s^{-1})	With	−0.11	−0.11	1.03	−0.98	−0.24	−0.91			
Primary	$v_{\rm pri,z}$ (km s^{-1})	Without	−0.27	−0.54	0.57	−1.52	−0.48	−0.09			
Secondary	$v_{\rm sec,z}$ (km s^{-1})	With	2.02	−1.19	−0.13	−0.65	−1.46	1.09			
Secondary	$v_{\rm sec,z}$ (km s^{-1})	Without	1.85	−1.04	0.21	0.39	−1.18	−0.16			

the polynomial given in Equation (B1) so that it is parallel to the x-axis after the rotation. To avoid confusion with the xyz-coordinates used in the transport, we refer to these new components as parallel (x-axis) and perpendicular components ($\perp1$—y-axis, $\perp2$—z-axis). The individual velocities of the test particles at 100 au are rotated using this transformation separately for each entry position. In the rotated frame and after subtracting the position-specific bulk velocity, we assume that the velocity distribution function does not depend on the entry position. Similarly, as in Swaczyna et al. (2023a), we validate this assumption by visually inspecting the distribution functions obtained for five large sectors: one centered about the inflow line and four *flank sectors* around it. We did not find statistically significant deviations in the distribution properties among these sectors. Finally, as we have limited statistics of trajectories, we assume that the velocity components in the rotated frame are independent. Therefore, the distribution function can be calculated as a product of three functions applied to each component separately:

$$f(v_\parallel, v_{\perp1}, v_{\perp2}) = f_\parallel(v_\parallel) f_{\perp1}(v_{\perp1}) f_{\perp2}(v_{\perp2}). \quad \text{(B2)}$$

As in the analysis of the ISN helium (Swaczyna et al. 2023a), we try to find the analytic functions that can describe each component. We identified the forms that provide a satisfactory reconstruction of the distribution function by using different forms including the (symmetric) kappa distribution and the generalized asymmetric kappa distribution defined in (Swaczyna et al. 2021). For the primary population, the parallel and first perpendicular ($\perp1$) components are well represented by the generalized asymmetric kappa distribution. This distribution peaks at speed u and is described by different temperatures and kappa indices on each side of the peak. For this asymmetric distribution function, the peak velocity u differs from zero so that the resulting bulk velocity is zero in the frame comoving with the population. The second perpendicular ($\perp2$), due to the symmetry of the problem, is described by the (symmetric) kappa distribution. The parameters of the fit functions are provided in Table 3. Note that the reported speeds are in the reference frame comoving with the population at the entrance point, i.e., the bulk speed is subtracted.

Table 3
Parameters of the Primary ISN Hydrogen Distribution at 100 au

Component	AS	u (km s^{-1})	T_1 (K)	κ_1 (1)	T_2 (K)	κ_2 (1)
$v_\parallel$	With	0.21	7910	18.7	7213	∞
$v_\parallel$	Without	−0.89	5220	∞	7139	∞
$v_{\perp1}$	With	0.03	8670	86	8515	∞
$v_{\perp1}$	Without	−0.18	7340	116	7856	38
$v_{\perp2}$	With	$\equiv0$	8280	∞	$\equiv T_1$	$\equiv\kappa_1$
$v_{\perp2}$	Without	$\equiv0$	7500	77	$\equiv T_1$	$\equiv\kappa_1$

As for helium (see Swaczyna et al. 2023a), the parallel component of the secondary ISN hydrogen population cannot be well described, even by the asymmetric kappa distribution. Therefore, following the procedure applied for helium, we describe this population as a superposition of four Maxwell distributions. However, the perpendicular components can be approximated by the kappa distributions. Table 4 shows the obtained parameters. The parameter ζ provides the relative weight of the normalized Maxwell distributions contributing to the parallel components. Figures 1 and 2 in Section 2 compare the obtained histograms with the distribution functions derived above and the Maxwell approximation of each function. The distributions are non-Maxwellian. Nevertheless, the temperatures and kappa indices do not represent their thermodynamical meanings but are merely used to approximate the distribution function effectively. Following the procedure outlined in Swaczyna et al. (2023a), we visually inspected the two-dimensional residual obtained after subtracting the product of the analytic functions from the numerical distribution function, which, similarly as in the case of helium, are small. Finally, the analytic functions are used to provide a numerical form for transport from 100 to 1 au, as described in Section 3.

Table 4
Parameters of the Secondary ISN Hydrogen Distribution at 100 au

Component	AS	ζ (1)	u (km s^{-1})	T_1 (K)	κ_1 (1)	T_2 (K)	κ_2 (1)
$v_{\parallel}(1)$	With	0.096	−11.44	1570	⋯	⋯	⋯
$v_{\parallel}(2)$	With	0.302	−4.36	3730	⋯	⋯	⋯
$v_{\parallel}(3)$	With	0.498	3.33	7950	⋯	⋯	⋯
$v_{\parallel}(4)$	With	0.104	7.07	13,030	⋯	⋯	⋯
$v_{\parallel}(1)$	Without	0.036	−12.6	830	⋯	⋯	⋯
$v_{\parallel}(2)$	Without	0.246	−6.89	2960	⋯	⋯	⋯
$v_{\parallel}(3)$	Without	0.407	0.24	5810	⋯	⋯	⋯
$v_{\parallel}(4)$	Without	0.312	6.49	9670	⋯	⋯	⋯
$v_{\perp 1}$	With	≡1	0.32	12,540	18	11,580	16
$v_{\perp 1}$	Without	≡1	0.05	12,290	18	12,020	23
$v_{\perp 2}$	With	≡1	≡0	9970	12	$\equiv T_1$	$\equiv \kappa_1$
$v_{\perp 2}$	Without	≡1	≡0	9910	12	$\equiv T_1$	$\equiv \kappa_1$

ORCID iDs

F. Rahmanifard https://orcid.org/0000-0001-9316-0553
P. Swaczyna https://orcid.org/0000-0002-9033-0809
E. J. Zirnstein https://orcid.org/0000-0001-7240-0618
J. Heerikhuisen https://orcid.org/0000-0001-7867-3633
A. Galli https://orcid.org/0000-0003-2425-3793
J. M. Sokół https://orcid.org/0000-0002-4173-3601
N. A. Schwadron https://orcid.org/0000-0002-3737-9283
E. Möbius https://orcid.org/0000-0002-2745-6978
D. J. McComas https://orcid.org/0000-0001-6160-1158
S. A. Fuselier https://orcid.org/0000-0003-4101-7901

References

Baranov, V. B., & Malama, Y. G. 1993, JGR, 98, 15157
Bzowski, M., Czechowski, A., Frisch, P. C., et al. 2019, ApJ, 882, 60
Bzowski, M., & Heerikhuisen, J. 2020, ApJ, 888, 24
Bzowski, M., Kubiak, M. A., Hłond, M., et al. 2014, A&A, 569, A8
Bzowski, M., Möbius, E., Tarnopolski, S., Izmodenov, V. V., & Gloeckler, G. 2008, A&A, 491, 7
Bzowski, M., Swaczyna, P., Kubiak, M. A., et al. 2015, ApJS, 220, 28
Fraternale, F., Pogorelov, N. V., & Bera, R. K. 2023, ApJ, 946, 97
Fuselier, S. A., Bochsler, P., Chornay, D., et al. 2009, SSRv, 146, 117
Galli, A., Wurz, P., Rahmanifard, F., et al. 2019, ApJ, 871, 52
Gloeckler, G., Möbius, E., Geiss, J., et al. 2004, A&A, 426, 845
Heerikhuisen, J., Florinski, V., & Zank, G. P. 2006, JGRA, 111, A06110
Heerikhuisen, J., Gamayunov, K. V., Zirnstein, E. J., & Pogorelov, N. V. 2016, ApJ, 831, 137
Heerikhuisen, J., Pogorelov, N. V., Florinski, V., Zank, G. P., & Kharchenko, V. 2009, in ASP Conf. Ser. 406, Numerical Modeling of Space Plasma Flows: ASTRONUM-2008, ed. Nikolai V. Pogorelov et al. (San Francisco, CA: ASP), 189
Izmodenov, V., Alexashov, D., & Myasnikov, A. 2005, A&A, 437, 35
Izmodenov, V. V., & Alexashov, D. B. 2015, ApJS, 220, 32
Izmodenov, V. V., & Alexashov, D. B. 2020, A&A, 633, 12
Izmodenov, V. V., Gruntman, M., & Malama, Y. G. 2001, JGR, 106, 10681
Katushkina, O. A., Galli, A., Izmodenov, V. V., & Alexashov, D. B. 2021, MNRAS, 501, 1633
Katushkina, O. A., Izmodenov, V. V., Alexashov, D. B., Schwadron, N. A., & McComas, D. J. 2015, ApJS, 220, 33
Kowalska-Leszczynska, I., Bzowski, M., Sokół, J. M., & Kubiak, M. A. 2018a, ApJ, 868, 49
Kowalska-Leszczynska, I., Bzowski, M., Sokół, J. M., & Kubiak, M. A. 2018b, ApJ, 852, 115
Kowalska-Leszczynska, I., Kubiak, M. A., & Bzowski, M. 2022, ApJ, 926, 27
Kubiak, M. A., Swaczyna, P., Bzowski, M., et al. 2016, ApJS, 223, 25
Lallement, R., & Bertin, P. 1992, A&A, 266, 479
Lee, M. A., Kucharek, H., Möbius, E., et al. 2012, ApJS, 198, 10
Lee, M. A., Möbius, E., & Leonard, T. W. 2015, ApJS, 220, 23
Lemaire, P., Vial, J. C., Curdt, W., Schühle, U., & Wilhelm, K. 2015, A&A, 581, A26
Lindsay, B. G., & Stebbings, R. F. 2005, JGR, 110, A12213
Linsky, J. L., Brown, A., Gayley, K., & Diplas, A. 1993, ApJ, 402, 694
Malama, Y. G. 1991, Ap&SS, 176, 21
McComas, D. J., Alexashov, D. B., Bzowski, M., et al. 2012, Sci, 336, 1291
McComas, D. J., Allegrini, F., Bochsler, P., et al. 2009, Sci, 326, 959
McComas, D. J., Bzowski, M., Fuselier, S. A., et al. 2015, ApJS, 220, 22
McComas, D. J., Christian, E. R., Schwadron, N. A., et al. 2018, SSRv, 214, 116
Möbius, E., Bochsler, P., Bzowski, M., et al. 2009, Sci, 326, 969
Möbius, E., Bzowski, M., Chalov, S., et al. 2004, A&A, 426, 897
Ovchinnikov, S. Y., Kamyshkov, Y., Zaman, T., & Schultz, D. R. 2017, JPhB, 50, 085204
Pogorelov, N. V., Heerikhuisen, J., Zank, G. P., & Borovikov, S. N. 2009, SSRv, 143, 31
Rahmanifard, F., Möbius, E., Schwadron, N., et al. 2019, ApJ, 887, 217
Ripken, H. W., & Fahr, H. J. 1983, A&A, 122, 181
Saul, L., Bzowski, M., Fuselier, S., et al. 2013, ApJ, 767, 130
Saul, L., Wurz, P., Rodriguez, D., et al. 2012, ApJS, 198, 14
Schultz, D. R., Ovchinnikov, S. Y., Stancil, P. C., & Zaman, T. 2016, JPhB, 49, 084004
Schwadron, N. A., Möbius, E., Leonard, T., et al. 2015, ApJS, 220, 25
Schwadron, N. A., Möbius, E., McComas, D. J., et al. 2016, ApJ, 828, 81
Schwadron, N. A., Möbius, E., McComas, D. J., et al. 2022, ApJS, 258, 7
Schwadron, N. A., Moebius, E., Kucharek, H., et al. 2013, ApJ, 775, 86
Sokół, J. M., & Bzowski, M. 2014, arXiv:1411.4826
Sokół, J. M., Bzowski, M., Tokumaru, M., Fujiki, K., & Mccomas, D. J. 2013, SoPh, 285, 167
Sokół, J. M., Kubiak, M. A., Bzowski, M., Möbius, E., & Schwadron, N. A. 2019, ApJS, 245, 28
Sokół, J. M., McComas, D. J., Bzowski, M., & Tokumaru, M. 2020, ApJ, 897, 179
Swaczyna, P., Bzowski, M., Fuselier, S. A., et al. 2023b, ApJS, 266, 2
Swaczyna, P., Bzowski, M., Heerikhuisen, J., et al. 2023c, ApJ, 953, 107
Swaczyna, P., Kubiak, M. A., Bzowski, M., et al. 2022a, ApJS, 259, 42
Swaczyna, P., McComas, D. J., Zirnstein, E. J., & Heerikhuisen, J. 2019, ApJ, 887, 223
Swaczyna, P., Rahmanifard, F., Zirnstein, E. J., & Heerikhuisen, J. 2023a, ApJ, 943, 74
Swaczyna, P., Rahmanifard, F., Zirnstein, E. J., McComas, D. J., & Heerikhuisen, J. 2021, ApJL, 911, L36
Swaczyna, P., Schwadron, N. A., Möbius, E., et al. 2022b, ApJL, 937, L32
Vallerga, J., Lallement, R., Lemoine, M., Dalaudier, F., & McMullin, D. 2004, A&A, 426, 855
Witte, M. 2004, A&A, 426, 835
Wood, B. E., Müller, H. R., Bzowski, M., et al. 2015, ApJS, 220, 31
Wurz, P., Saul, L., Scheer, J. A., et al. 2008, JAP, 103, 054904
Wurz, P., Schletti, R., & Aellig, M. R. 1997, SurSc, 373, 56
Zank, G. P., Heerikhuisen, J., Wood, B. E., et al. 2013, ApJ, 763, 20
Zirnstein, E. J., Heerikhuisen, J., Funsten, H. O., et al. 2016, ApJL, 818, L18
Zirnstein, E. J., Heerikhuisen, J., McComas, D. J., & Schwadron, N. A. 2013, ApJ, 778, 112